AGU PUBLICATIONS

JGR

Journal of Geophysical Research: Space Physics

RESEARCH ARTICLE
10.1002/2015JA021858

Special Section:
Inner Magnetosphere Coupling: Recent Advances

Testing the magnetotail configuration based on observations of low-altitude isotropic boundaries during quiet times

R. Ilie[1], N. Ganushkina[1,2], G. Toth[1], S. Dubyagin[2], and M. W. Liemohn[1]

[1]Climate and Space, University of Michigan, Ann Arbor, Michigan, USA, [2]Finish Meteorological Institute, Helsinki, Finland

Key Points:
- We tested the threshold condition for strong pitch angle scattering based on the MHD magnetic field
- SWMF model suggests a threshold condition for strong pitch angle scattering of k = 33
- For quiet time, the k parameter varies within 2 orders of magnitude

Correspondence to:
R. Ilie,
rilie@umich.edu

Citation:
Ilie, R., N. Ganushkina, G. Toth, S. Dubyagin, and M. W. Liemohn (2015), Testing the magnetotail configuration based on observations of low-altitude isotropic boundaries during quiet times, *J. Geophys. Res. Space Physics*, *120*, doi:10.1002/2015JA021858.

Received 31 AUG 2015
Accepted 6 DEC 2015
Accepted article online 12 DEC 2015

Abstract We investigate the configuration of the geomagnetic field on the nightside magnetosphere during a quiet time interval based on National Oceanic and Atmospheric Administration Polar Orbiting Environment Satellites Medium Energy Proton and Electron Detector (NOAA/POES MEPED) measurements in combination with numerical simulations of the global terrestrial magnetosphere using the Space Weather Modeling Framework. Measurements from the NOAA/POES MEPED low-altitude data sets provide the locations of isotropic boundaries; those are used to extract information regarding the field structure in the source regions in the magnetosphere. In order to evaluate adiabaticity and mapping accuracy, which is mainly controlled by the ratio between the radius of curvature and the particle's Larmor radius, we tested the threshold condition for strong pitch angle scattering based on the MHD magnetic field solution. The magnetic field configuration is represented by the model with high accuracy, as suggested by the high correlation coefficients and very low normalized root-mean-square errors between the observed and the modeled magnetic field. The scattering criterion, based on the values of $k = \frac{R_c}{\rho}$ ratio at the crossings of magnetic field lines, associated with isotropic boundaries, with the minimum **B** surface, predicts a critical value of $k_{CR} \sim 33$. This means that, in the absence of other scattering mechanisms, the strong pitch angle scattering takes place whenever the Larmor radius is ~33 times smaller than the radius of curvature of the magnetic field, as predicted by the Space Weather Modeling Framework.

1. Introduction

Determining the geometry of the Earth's magnetic field under various solar wind and interplanetary magnetic field (IMF) conditions is crucial for understanding the connections between ionospheric and auroral features and magnetospheric phenomena. Knowledge of the configuration of the magnetic field lines is required in order to understand the magnetic mapping in different conditions and between different regions of the near-Earth space.

Isotropic boundaries (IBs) have been proposed as proxies to estimate the degree of magnetic field stretching in the magnetotail [e.g., *Sergeev et al.*, 1993; *Sergeev and Gvozdevsky*, 1995; *Meurant et al.*, 2007] and have been the subject of numerous studies [e.g., *Sergeev and Tsyganenko*, 1982; *Tsyganenko*, 1982; *Sergeev et al.*, 1983; *Buechner and Zelenyi*, 1987; *Sergeev et al.*, 1994; *Delcourt et al.*, 1996; *Donovan et al.*, 2003b; *Ganushkina et al.*, 2005; *Lvova et al.*, 2005; *Kubyshkina et al.*, 2009; *Dubyagin et al.*, 2013]. They are interpreted as the separation between the adiabatic and stochastic particle motion in the tail current sheet, since they correspond to locations where the locally trapped and the precipitated fluxes of energetic particles are comparable [*Fritz*, 1970] and characterize the transition from weak precipitation rate to isotropic precipitation in the high-latitude region. In the regions where the magnetic field line curvature becomes comparable to the particle gyroradius, significant pitch angle scattering occurs [*Tsyganenko*, 1982; *Buechner and Zelenyi*, 1987; *Delcourt et al.*, 1996]. *Blockx et al.* [2005, 2007] showed that the SI12 camera on board the IMAGE spacecraft [*Sandel et al.*, 2000] was an excellent tool to remotely determine the position of the isotropy boundary in the ionosphere and thus was able to provide a reasonable estimate of the amount of magnetic field stretching in the magnetotail.

The isotropic boundary depends only on the equatorial magnetic field and the particle rigidity. The usefulness of the IB location as an indicator of the tail current characteristics was suggested by *Sergeev et al.* [1993], who showed that the measured IB latitude correlates very well with the magnetic field direction measured by GOES satellite at geostationary orbit near the tail current sheet. The magnetic inclination angle in the tail near

the current sheet decreases as the measured IB latitude decreases; that is, when the magnetic field becomes more stretched, the IB shifts to lower latitudes. Since by Ampere's law the tangent of the magnetic inclination angle is approximately inversely proportional to the linear current density in the Y_{GSM} direction, the inverse of the IB latitude reflects the intensity of the current at the near-Earth tail.

Isotropic boundaries for ions were observed at all MLTs and all activity conditions. The IB latitudes depend on the particle species, energy, MLT, and magnetic activity and for a given species, the higher the energy, the lower the latitude at which the IB is observed [*Sergeev et al.*, 1993; *Sergeev and Gvozdevsky*, 1995]. These boundaries often present dispersion patterns and could potentially be as broad as ~1° [*Sergeev et al.*, 2015]. However, reversed energy-latitude dispersion patterns also have been observed [*Donovan et al.*, 2003a]. These lower energy ion precipitation boundaries that extend to lower latitude than the higher-energy ion precipitation have been associated with scattering by the electromagnetic ion cyclotron (EMIC) waves. It has been suggested that the scattering due to wave-particle interactions is most effective in the plasma tubes extending ~1 R_E earthward from the boundary that separates adiabatic and stochastic particle motion [*Sergeev et al.*, 2015].

The location of the IB could also place a lower bound on the mapping of the substorm onset location [*Gilson et al.*, 2011, 2012]. *Sergeev and Gvozdevsky* [1995] derived the so-called MT-index [further developed by *Asikainen et al.* 2010], from the observed position (latitude and MLT) of the IB of 100 keV protons. This index characterizes the large-scale tailward stretching of the magnetic field lines in the magnetotail at 5–10 R_E distances and it changes approximately linearly with changes of the magnetic field and inclination at the geostationary orbit at midnight. A semiempirical model derived by *Asikainen et al.* [2010] describes the contributions of the ring, tail, and magnetopause currents to the *Dst* index parameterized by solar wind and IMF parameters and by the observed IB latitudes.

Continuous measurements on NOAA satellites can provide, though indirectly, valuable information about the dynamics of the magnetotail. The extensive NOAA/POES MEPED low-altitude data sets provide the locations of isotropic boundaries (IB) that are used to learn about particle distributions and field structure in the source regions in the magnetosphere [*Sergeev et al.*, 1993; *Ganushkina et al.*, 2005; *Lvova et al.*, 2005; *Kubyshkina et al.*, 2009].

The only way to determine the magnetic field configuration in the entire magnetosphere is to use an existing model. Empirical models such as the most widely used Tsyganenko models [e.g., *Tsyganenko*, 1995, 2002; *Tsyganenko and Sitnov*, 2005] based on tens of years of satellite data or models based on analytical relations describing the dynamics of different magnetic field sources dependent on input parameters [*Alexeev et al.*, 2001], provide magnetospheric configurations corresponding to average conditions. Event-oriented models developed to provide a realistic representation of the magnetospheric magnetic field during geomagnetic storms are most suitable for postanalysis of specific events [*Ganushkina et al.*, 2004, 2010]. A global representation of the magnetic field can also be obtained based on first principles (such as MHD), self-consistently coupled numerical models.

For this study, we analyze the NOAA/POES MEPED data during the 13 February 2009 quiet time period, in combination with first-principles-based simulations with the Space Weather Modeling Framework [SWMF and the models coupled therein *Tóth et al.*, 2005, 2012] in order to determine what is the strong scattering threshold condition based on magnetic field representation as described by the SWMF model. That is, we test the conditions when the nightside particle precipitation is dominated by field line curvature scattering of central plasma sheet particles into the loss cone without including wave-particle interactions.

The article is organized as follows: In sections 2 and 3 we present an overview of the time interval investigated and the observations of the isotropy boundaries, respectively. Section 4 presents the description of the model, while its validation is presented in section 5. The results of mapping the isotropic boundaries are shown in sections 6 and 7. Discussion and conclusions are presented in sections 8 and 9, respectively.

2. Overview of the Quiet Time Interval: 13 February 2009

We apply our methodology to a 24 h long quiet time interval, 13 February 2009, which was selected based on the availability of magnetic field observations on the nightside magnetosphere. During this time, magnetic field data were available from the GOES, Cluster, Geotail, and THEMIS spacecraft.

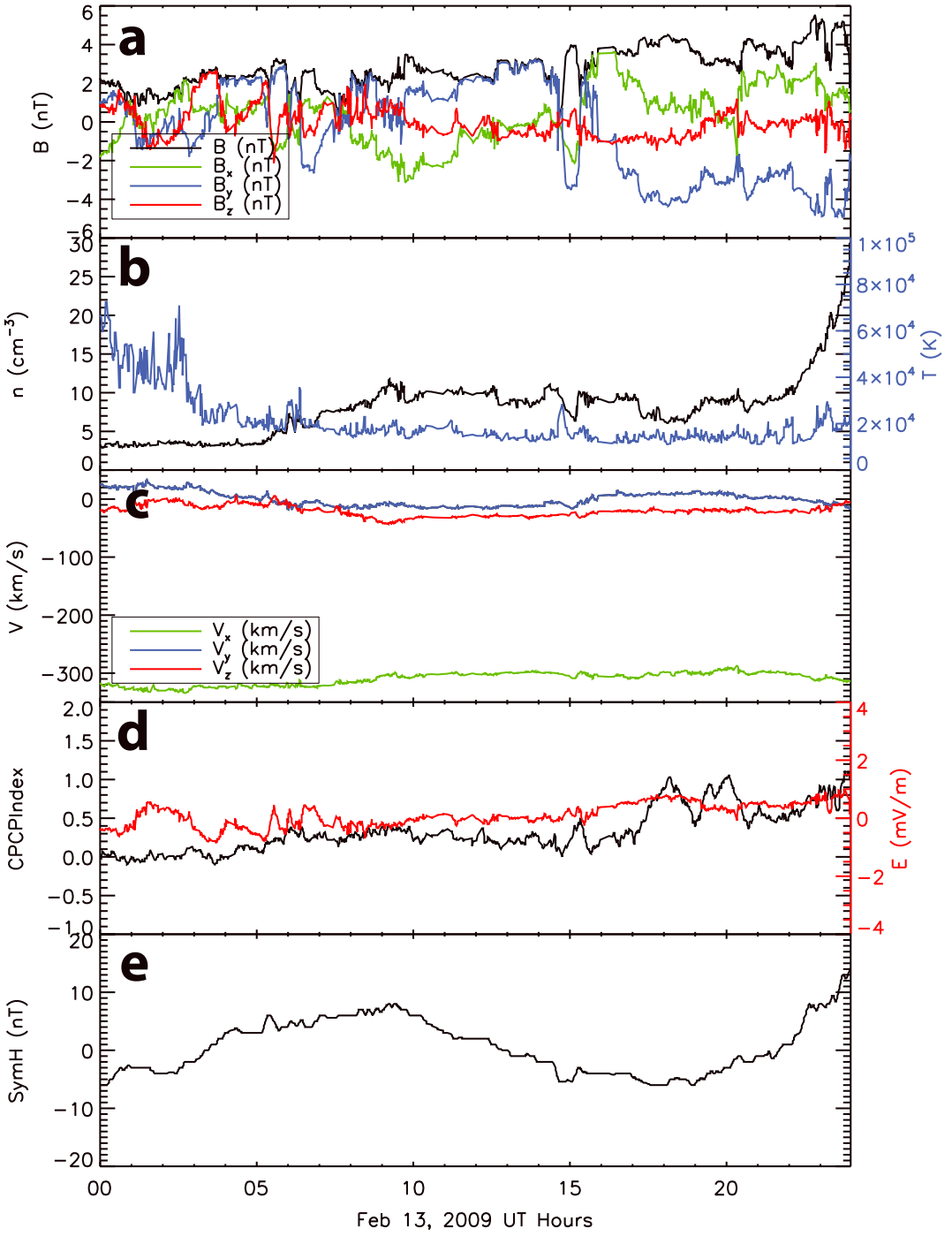

Figure 1. The 13 February 2009 event parameters. (a) All components of the interplanetary magnetic field (B_x, green line; B_y, blue line; B_z, red line; and B magnitude (black line)). (b) The solar wind number density (block line) and temperature (blue line). (c) All components of the solar wind velocity (V_x, green line; V_y, blue line; and V_z, red line) followed by the (d) electric field (red line) and CPCP Index (black line). (e) The *Sym-H* index throughout this period.

The initial selection of a quiet time period was prompted by the fact that during undisturbed conditions, the probability of scattering due to particle interactions with electromagnetic waves is small, since waves are predominantly present in the inner magnetosphere during the periods of the increased magnetospheric activity [*Halford et al.*, 2010; *Braysy et al.*, 1998; *Usanova et al.*, 2012]. Furthermore, the effect of inductive and impulsive electric fields that could further accelerate particles is less significant during undisturbed times and the distribution of trapped particles around drift shells is most likely uniform during quiet times.

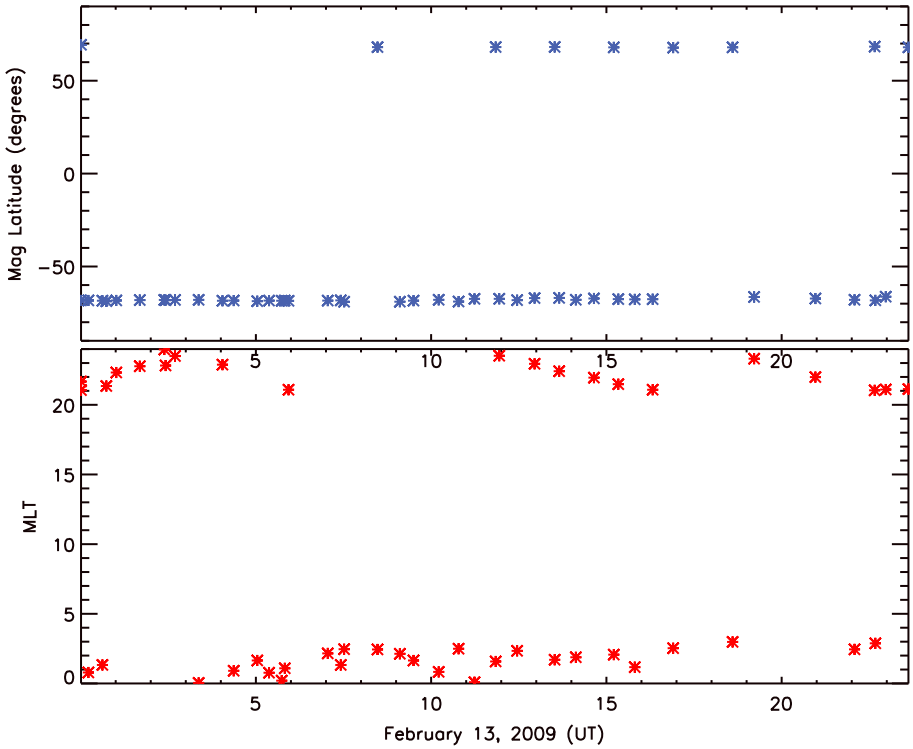

Figure 2. Locations of isotropic boundaries during 13 February 2009 observed by all available NOAA-POES satellites as a function of (a) magnetic latitude and (b) magnetic local time.

Figure 1 presents the overview of the quiet interval. From top to bottom we show the solar wind parameters from ACE spacecraft, the interplanetary magnetic field, the solar wind number density and temperature, the solar wind velocity vector, and the electric field. The following panels show the Cross Polar Cap Potential (CPCP) and *SYM-H* indices throughout this time interval obtained from the OMNI database. The IMF B_z hovers around zero, with a minimum excursion at −2 nT, indicative of a weak geo-effectiveness. The solar wind particle density is less than 10 cm^{-3} throughout the entire day, and the earthward solar wind velocity stays within a nominal range (~300 km/s). Also, the CPCP and *SYM-H* indices are indicative of quiet time since both display very small variations and magnitudes. Furthermore, inspection of ground-based observations reveals no wave activity between 2100 and 0300 MLT during this time (M. Usanova, personal communication, 2015).

3. Observations of Isotropic Boundaries

The data from the Medium Energy Proton and Electron Detector (MEPED) on board the National Oceanic and Atmospheric Administration Polar Orbiting Environment Satellites (NOAA/POES) is used to determine IB locations. NOAA/POES satellites have nearly circular orbits with altitude of 850 km and orbital period of 100 min crossing the auroral oval 4 times per orbit with just over 14 orbits in a day.

The MEPED detector has two telescopes measuring fluxes of trapped particles and those precipitating into the loss cone allowing IB determination. The fluxes are measured in several energy bands for ions (ranging from 30 to 6900 keV), which are assumed to be protons. This study is based on data from the first proton energy band, referred to as P1 (30–80 keV), but we also inspected the higher-energy channels to exclude the events with anomalous energy-latitude dispersion.

We use the IB determination procedure described in detail by *Dubyagin et al.* [2013] which outputs the IB position and the uncertainty interval. Assuming that the satellite moves from the equator to the pole, the equatorial boundary is defined as the polewardmost point where $F^0/F^{90} < 0.5$ and this condition is fulfilled for the four preceding points (8 s interval); the polar boundary is the first point after the equatorial boundary where $F^0/F^{90} > 0.75$ and $F^0/F^{90} > 0.75$ for four subsequent points, where F^0 and F^{90} correspond to the precipitating and the trapped flux, respectively. The IB uncertainty interval was selected so that it ignores brief periods of isotropic or nearly isotropic fluxes at the equatorial part of the auroral oval, which could be

Table 1. THEMIS and NOAA Conjugacies for Isotropic Boundaries Observations During the 13 February 2009 Period

Spacecraft/Time	Plane	k	B_{min}(nT)	$X(R_e)$	$Y(R_e)$	$Z(R_e)$	$R_c(R_e)$	Conj. With
METOP 02/01:41:16	Minimum B	38.45	71.45	−6.71	2.10	−2.07	2.12	THEMIS A, D
METOP 02/01:41:16	SM Z=0	38.44	72.94	−6.57	2.11	−2.45	2.18	THEMIS A, D
METOP 02/03:22:00	Minimum B	39.00	75.60	−6.53	−0.26	−2.24	2.03	THEMIS A, D, E
METOP 02/03:22:00	SM $Z = 0$	39.03	75.90	−6.47	−0.27	−2.79	2.04	THEMIS A, D, E
NOAA 16/02:23:16	Minimum B	30.71	64.59	−6.89	−0.15	−2.45	1.91	THEMIS A, D, E
NOAA 16/02:23:16	SM $Z = 0$	30.70	63.01	−6.78	−0.13	−2.72	1.97	THEMIS A, D, E
NOAA 16/02:25:23	Minimum B	27.62	56.70	−6.80	2.02	−2.38	1.91	THEMIS A, E
NOAA 16/02:25:23	SM $Z = 0$	27.62	56.69	−6.67	2.03	−2.68	2.00	THEMIS A, E
NOAA 17/02:41:34	Minimum B	28.49	58.96	−6.86	0.72	−2.54	1.90	THEMIS A, D, E
NOAA 17/02:41:34	SM $Z = 0$	28.48	59.88	−6.75	0.73	−2.78	1.96	THEMIS A, D, E
NOAA 17/04:22:02	Minimum B	44.10	80.97	−6.29	−1.79	−2.70	2.14	THEMIS A, E
NOAA 17/04:22:02	SM $Z = 0$	44.10	81.10	−6.24	−1.79	−2.80	2.15	THEMIS A, E
NOAA 18/16:54:17	Minimum B	43.80	88.18	−5.39	−4.21	−0.11	1.95	THEMIS A, E
NOAA 18/16:54:17	SM $Z = 0$	43.80	88.31	−5.38	−4.21	−0.21	1.96	THEMIS A, E

caused by a wave-particle interaction scattering mechanism, and the the inaccuracy was less than 0.3 degree for selected events.

For the selected event, we obtained the set of IB locations from all NOAA satellites. Figure 2 shows their dependence on magnetic latitude and magnetic local time (MLT) and their evolution with time. During this quiet period, there was very little variation for the location of the isotropic boundaries with magnetic latitude, most of them originating from magnetic latitudes above 60°. Even though they were observed at all MLTs, we only selected the ones that were identified to reside on the night sector between 2100 and 0300 MLT. Figure 2 only shows the IB locations considered in this study. In addition, to exclude the possible wave-particle-interaction-induced IBs, we inspected the IBs for the higher-energy channels (P2, P3) to make sure that there is no anomalous energy-latitude dispersion. We focus here only on the observations of isotropic boundaries at times when the THEMIS A, D, and E spacecraft were located in the same MLT sector (±1 h) as the NOAA satellites and at radial distances $r = 7–10\ R_E$. To determine the threshold condition for strong pitch angle scattering requires reasonable knowledge of the local magnetic field. That being said, the comparison with the THEMIS observations, which were on the same MLT sector with the NOAA satellites, ensures that the magnetic field in that region is well described by the model. The event selection was made to maximize the opportunity for such conjugacies; therefore, the seven conjugate observations constitute the entire set available at this time and these observations are summarized in Table 1.

4. Methodology: Model Specifications

The numerical simulations presented here were performed using the Space Weather Modeling Framework (SWMF) [*Tóth et al.*, 2005, 2012] developed at University of Michigan. This framework is a robust numerical tool for heliophysical simulations, providing a high-performance computational capability to simulate the physics from the solar surface to the upper atmosphere of the Earth. It contains numerical modules for numerous physics domains, with a state of the art model solving the physics within each domain. The physical domains included in the simulations presented here are: the Global Magnetosphere (GM), Ionosphere Electrodynamics (IE) and Inner Magnetosphere (IM). The following is a brief description of each of the components.

4.1. Global Magnetosphere

The GM domain is represented by the Block Adaptive Tree Solar-wind-type Roe Upwind Scheme (BATS-R-US) global magnetohydrodynamic (MHD) model [*Powell et al.*, 1999; *Tóth et al.*, 2012] that solves for the transfer of mass and energy from the solar wind to the magnetosphere. This code solves the semirelativistic MHD equations [*Gombosi et al.*, 2002] with the option to include Hall effect terms [*Tóth et al.*, 2008], multifluid equations [*Glocer et al.*, 2009], and anisotropic plasma pressure [*Meng et al.*, 2012]. In the simulations described here, BATS-R-US is configured to solve the three-dimensional single-fluid MHD equations. This component provides the inner magnetosphere (IM) model, the field line volume in the whole IM domain, plasma density and temperature at the outer boundary, and the field-aligned currents' strength and location.

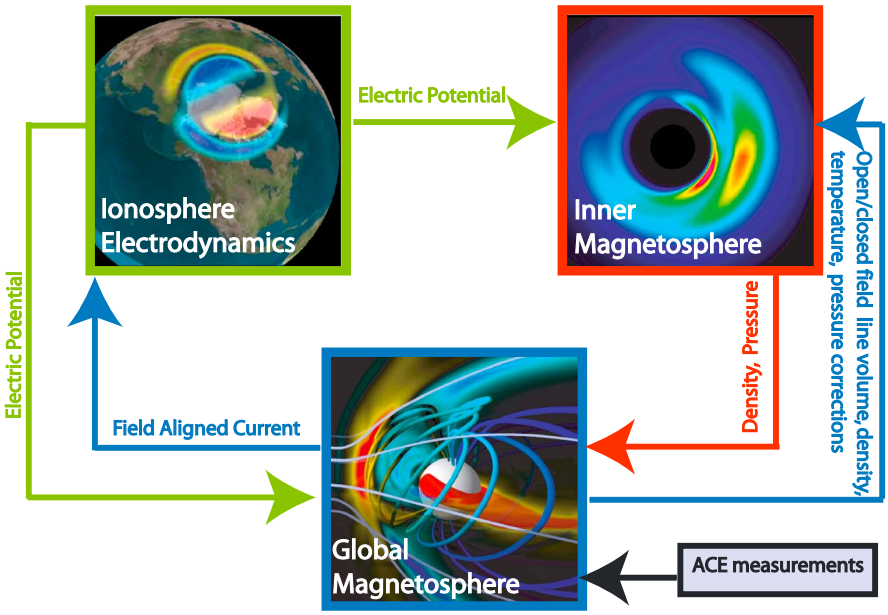

Figure 3. Coupling schematic of the model couplings within SWMF.

4.2. Inner Magnetosphere

The Rice Convection Model (RCM) [*Harel et al.*, 1981; *Toffoletto et al.*, 2003], the IM model used for this study, solves the energy-dependent particle flows of hot ions and electrons and describes the dynamic behavior of the inner magnetospheric particles in terms of isotropic fluids in the near-Earth region in the spatial domain bounded by closed magnetic field lines and populated by keV energy particles. The IM component provides the density and pressure along the magnetic field lines and feeds this information to the GM component so that the MHD results are corrected toward the IM results [*De Zeeuw et al.*, 2004], while BATS-R-US provides the RCM outer boundary as the dynamic, last closed magnetic field boundary. It has been the predominantly used code for SWMF storm studies [e.g., *Zhang et al.*, 2007; *Ilie et al.*, 2010a, 2010b; *Ganushkina et al.*, 2010; *Liemohn et al.*, 2011; *Ilie et al.*, 2010a, 2010b, 2013, 2015].

4.3. Ionospheric Electrodynamics

The two-dimensional electric potential and auroral precipitation patterns are described within this domain. The SWMF uses the ionospheric electrodynamics (IE) model of *Ridley and Liemohn* [2002] and *Ridley et al.* [2004] which consists of an electric potential solver and a model of the electron precipitation to calculate the height-integrated ionospheric quantities at an altitude of ~110 km. Calculations of the conductance pattern and particle precipitation are based on the field-aligned currents information passed from the GM component, while the electric potential is passed both to the IM and converted to velocity at the inner boundary of GM.

4.4. Simulation Setup

The message passing between these modules is done self-consistently through couplers inside the SWMF. Each of the models within SWMF has been extensively tested, validated,and used for scientific studies of the geospace. It has been used extensively to investigate the near-Earth space environment, investigating storm dynamics [*Zhang et al.*, 2007; *Ilie et al.*, 2010a, 2010b; *Ganushkina et al.*, 2010; *Ilie et al.*, 2013], solar wind-magnetosphere energy coupling [*Yu and Ridley*, 2009; *Ilie et al.*, 2010a, 2010b, 2013], and magnetosphere-ionosphere coupling [*Zhang et al.*, 2007; *Glocer et al.*, 2009; *Ilie et al.*, 2015]. An illustration of the modules and their coupling within the SWMF is presented in Figure 3.

The GM inner boundary, located at 2.5 Earth radius (R_E), is set with a passive source term in which the density is kept at a constant value and the radial velocity is set to zero. The value we use in this work (28 cm^{-3}) is the nominal value that has been tested and used in numerous SWMF simulations as the default inner boundary condition. This is further discussed in *Welling and Liemohn* [2014] which suggests that this boundary condition yields a physically reasonable outflow flux to the magnetosphere.

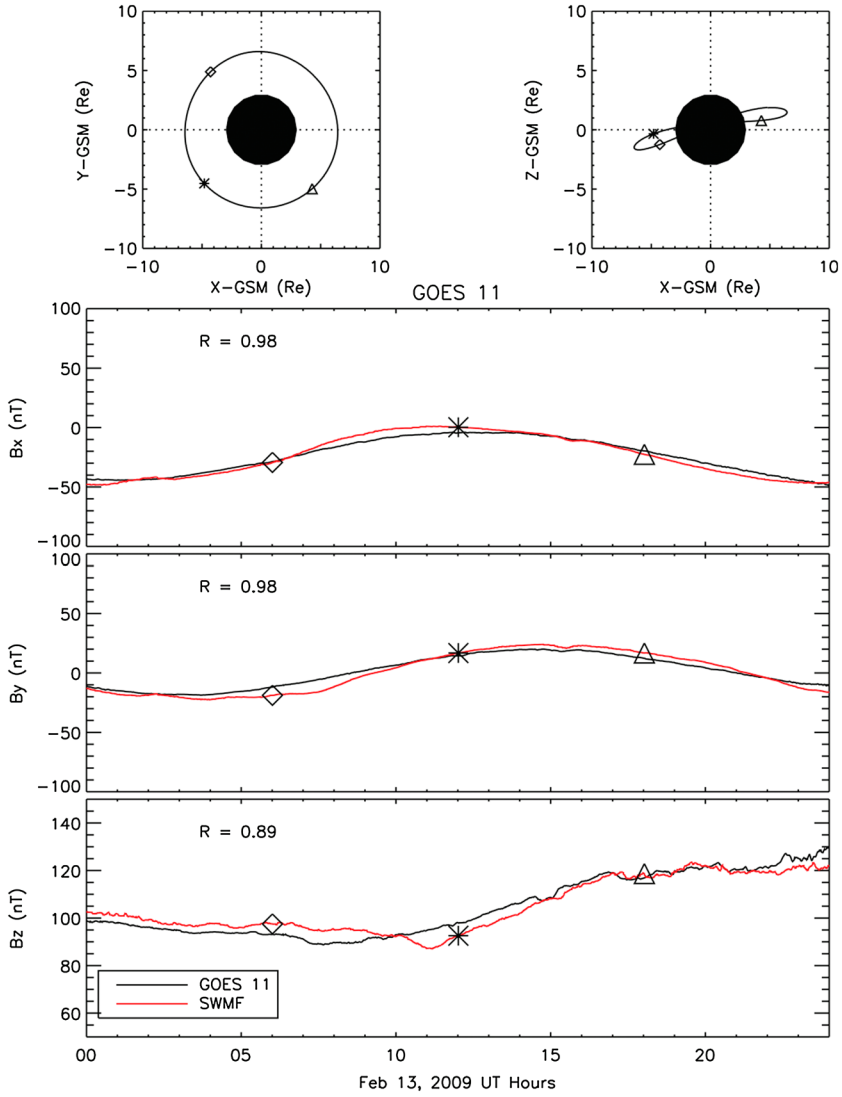

Figure 4. Comparison between the total magnetic field as output from SWMF magnetospheric modeling (red) and observed at GOES 11 (black) for 13 February 2009 interval. (top row) The spacecraft position in the $Y, Z = 0$ planes, followed by the magnetic field components as measured by the satellite (black lines) and predicted by the model (red lines). The green diamond, star and triangle are used to show the satellite position and progression during the time interval presented here. Correlation coefficients between the observed and simulated values of B_x, B_y, and B_z are indicated in each of the corresponding panels.

The GM used a Cartesian grid extending from 32 R_E upstream to 224 R_E downtail, 128 R_E in both y and z directions. The grid resolution varies from 1/8 R_E in the spherical shell 2.5 to 3.5 R_E close to the body, to 4 R_E near the outer edges of the domain using a total of about 4 million grid cells.

The simulation was first ran to reach steady state, using local time stepping for the first 2500 iterations with independent local time stepping within each cell from the BATS-R-US computation domain. This means that each cell uses a time step based on the local numerical stability criteria, allowing the BATS-R-US model to accelerate the convergence toward a steady state. After the steady state is reached, the simulation was allowed to run in the time accurate mode. The coupling frequency of GM with IM is 10 s while GM and IE exchange information at every 5 s. Note that the model setup does not account for wave-particle interactions. However, since during the interval studied here wave activity was not recorded, the models involved are appropriate for the problem investigated.

Table 2. Normalized Root-Mean-Square Errors (nRMSE) and Correlation Coefficients (R) Between the Simulated and Observed Magnetic Field Values

Spacecraft	nRMSE(B_x)	nRMSE(B_y)	nRMSE(B_z)	R(B_x)	$R(B_y)$	$R(B_z)$
Cluster 1	0.0064	0.0131	0.0087	0.890	0.929	0.809
Cluster 2	0.0061	0.0162	0.0087	0.873	0.890	0.802
Cluster 3	0.0013	0.0163	0.0048	0.700	0.860	0.782
Cluster 4	0.0071	0.0134	0.0094	0.877	0.905	0.809
Geotail	0.0815	0.0808	0.1397	0.985	0.934	0.952
GOES 11	0.0820	0.1136	0.0909	0.977	0.983	0.885
GOES 12	0.0538	0.0375	0.3083	0.994	0.995	0.713
THEMIS A	0.0073	0.0084	0.0095	0.923	0.921	0.970
THEMIS B	0.1994	0.1091	0.1340	0.736	0.738	0.444
THEMIS C	0.1190	0.0679	0.1192	0.926	0.774	0.708
THEMIS D	0.0157	0.0188	0.0122	0.962	0.881	0.965
THEMIS E	0.0086	0.0108	0.0095	0.961	0.959	0.967

5. SWMF Validation: Magnetic Field in the Tail

During the 13 February 2009, several spacecraft were probing the magnetic field on the nightside magnetosphere (GOES11, GOES12, Cluster1-4, Geotail, and THEMIS A–E). These particular satellites were virtually "flown" through the SWMF output, extracting the MHD parameters at the exact time and location of the spacecraft; therefore, one to one data-model comparison is possible.

Since both the radius of curvature and the particle gyroradius, and implicitly the k ratio, are dependent on the total magnetic field magnitude, we validate the magnetic field model results by comparing them with the corresponding in situ magnetic field observations available. Figures 4–7 show four selective examples for such comparison. In each figure, the satellite position in GSM coordinates is indicated in the top row and magnetic field components are presented in the following three rows. The black lines represent in situ measurements of the magnetic field vector, while the red lines show the simulated values for the same quantities extracted from the model output at the satellite location. Correlation coefficients between the observed and simulated values of B_x, B_y, and B_z are indicated in each of the corresponding panels.

To quantify the SWMF performance, we use the correlation coefficient and normalized root-mean-square error (nRMSE) (as defined in equation (1)) between each of the modeled and the observed magnetic field components.

$$\mathrm{nRMSE} = \sqrt{\frac{\sum_i^n (x_i - y_i)^2}{\sum_i^n x_i^2}} \tag{1}$$

where x represents the measured value, y represents the simulated value, and n corresponds to the number of data-model pairs used in the calculation. nRMSE ranges from 0, which means that the model is in perfect agreement with the observations, to 1. A value of 1 indicates that the simulation results are within ± 1 of the measured value means. Table 2 shows these values for these data-model comparisons. Note that for all the data-model comparisons the nRMSE scores are well below 0.2. In fact, most of the nRMSE are much smaller than 0.2, indicating that the model results are very close to the observed values for the corresponding parameters and the errors are much smaller than the average magnitude of the observations.

However, this value can be misleading; therefore, the nRMSE values must be paired with the correlation coefficients for a proper interpretation of these statistics. The correlation coefficients between the simulated and observed data sets, which measure how well the two sample populations vary together, reveal that the magnetic field configuration is modeled very well by the model, throughout this time period (see Table 2 for the entire matrix). The correlation coefficients are mostly above 0.7, except in the case of THEMIS B comparison between modeled and observed B_z (not shown here). In this case, the observed field shows noisy excursions

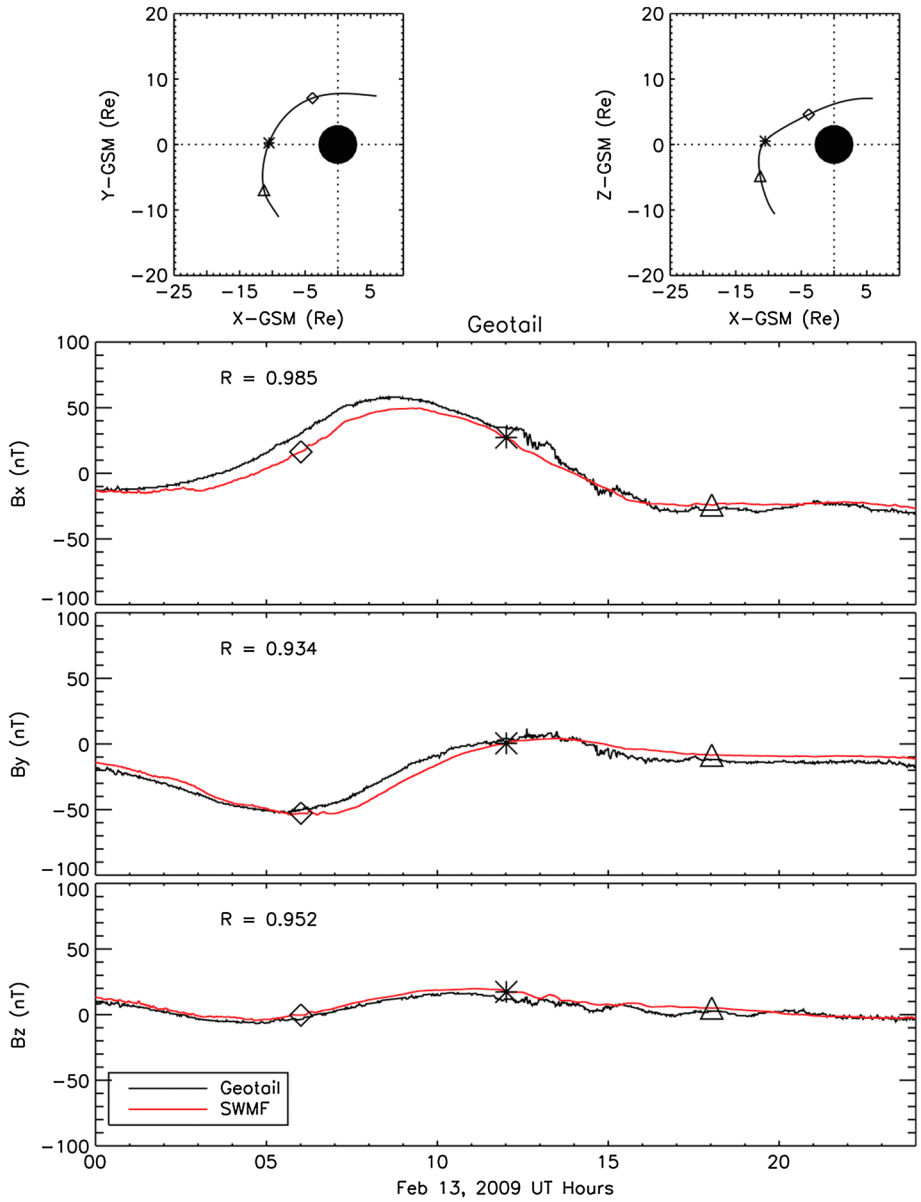

Figure 5. Comparison between the total magnetic field as output from SWMF magnetospheric modeling (red) and observed at Geotail (black) for 13 February 2009 interval. (top row) The spacecraft position in the $Y, Z = 0$ planes, followed by the magnetic field components as measured by the satellite (black lines) and predicted by the model (red lines). The green diamond, star, and triangle are used to show the satellite position and progression during the time interval presented here. Correlation coefficients between the observed and simulated values of B_x, B_y, and B_z are indicated in each of the corresponding panels.

around zero while the simulated value is much smoother. By running a moving average (with a window of 2 min) through the THEMIS B observed values of B_z, the correlation coefficient increases to a ~0.7 value.

The nRMSE together with the correlation coefficients analysis indicates that the magnetic field is modeled with high accuracy by the SWMF and that the model is capable of capturing the trends within the observations.

6. Mapping of the Isotropic Boundaries

We assume that there exists a robust and always operating pitch angle scattering in the magnetic field regions where the conditions for adiabatic particle motion are violated [*Tsyganenko*, 1982; *Buechner and Zelenyi*, 1987; *Delcourt et al.*, 1996]. In particular, if the effective Larmor radius ($\rho = \frac{mv}{qB}$, where m is the particle mass, v is the

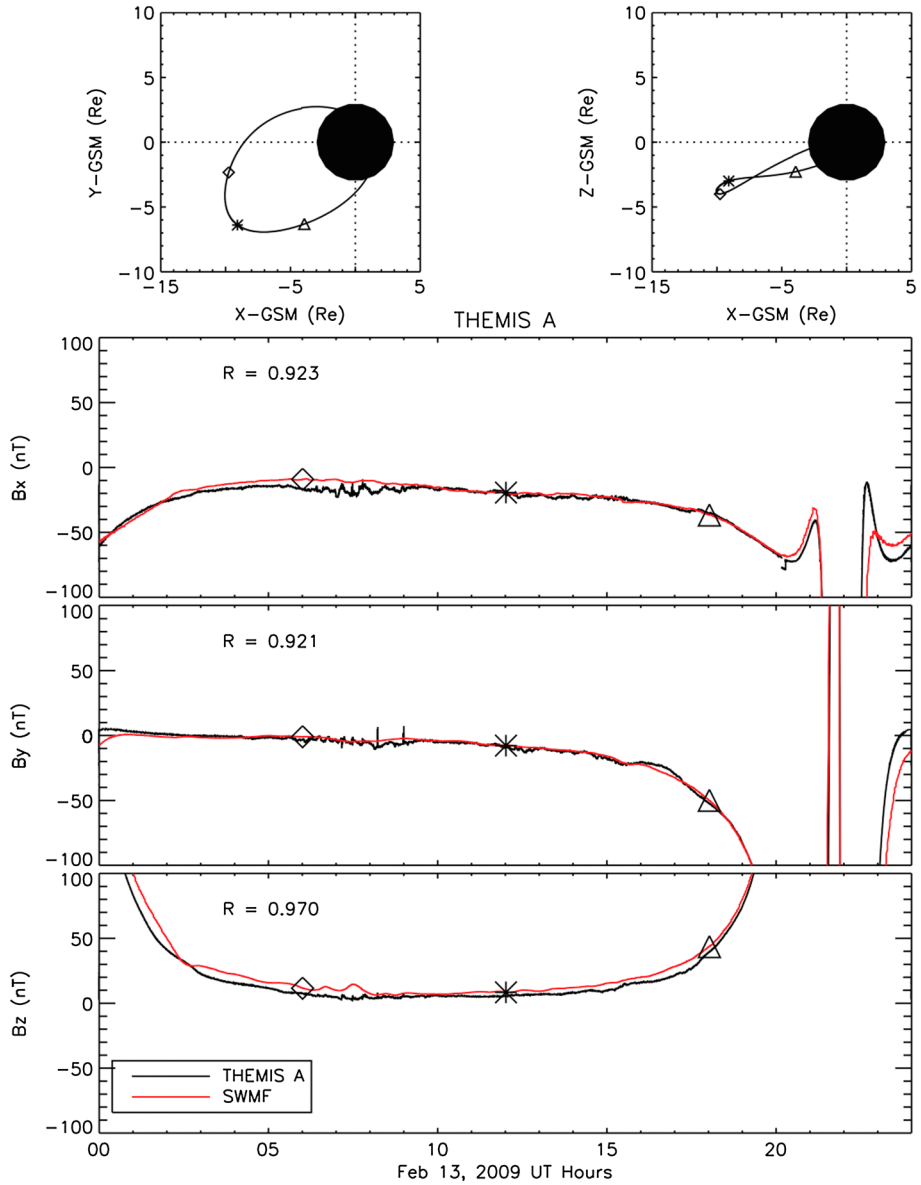

Figure 6. Comparison between the total magnetic field as output from SWMF magnetospheric modeling (red) and observed at THEMIS A (black) for 13 February 2009 interval. (top row) The spacecraft position in the $Y, Z = 0$ planes, followed by the magnetic field components as measured by the satellite (black lines) and predicted by the model (red lines). The green diamond, star, and triangle are used to show the satellite position and progression during the time interval presented here. Correlation coefficients between the observed and simulated values of B_x, B_y, and B_z are indicated in each of the corresponding panels.

total particle velocity, q is the particle charge, and B is the magnetic field) becomes comparable to the radius of the field line curvature R_c in the equatorial current sheet ($\frac{1}{R_c} = |(\vec{b} \cdot \nabla)\vec{b}|$, where $\vec{b}$ is the unit vector along the magnetic field direction), then the first adiabatic invariant is violated and pitch angle scattering occurs, allowing particles to be scattered into the loss cone. The scattering efficiency is controlled by the value of $k = \frac{Rc}{\rho}$, which depends on the current sheet structure and particle parameters, as well as on the required amplitude of the pitch angle change.

Using the magnetic field output from the SWMF, we determine the magnetic field lines for several nightside IBs locations and its crossing in the magnetotail at the surface defined by the minimum magnetic field ($B = B_{min}$) points along the magnetic field line. Please note that this event was selected to maximize the number of conjunctions with various satellites. There were only seven times when one of the available satellites in the

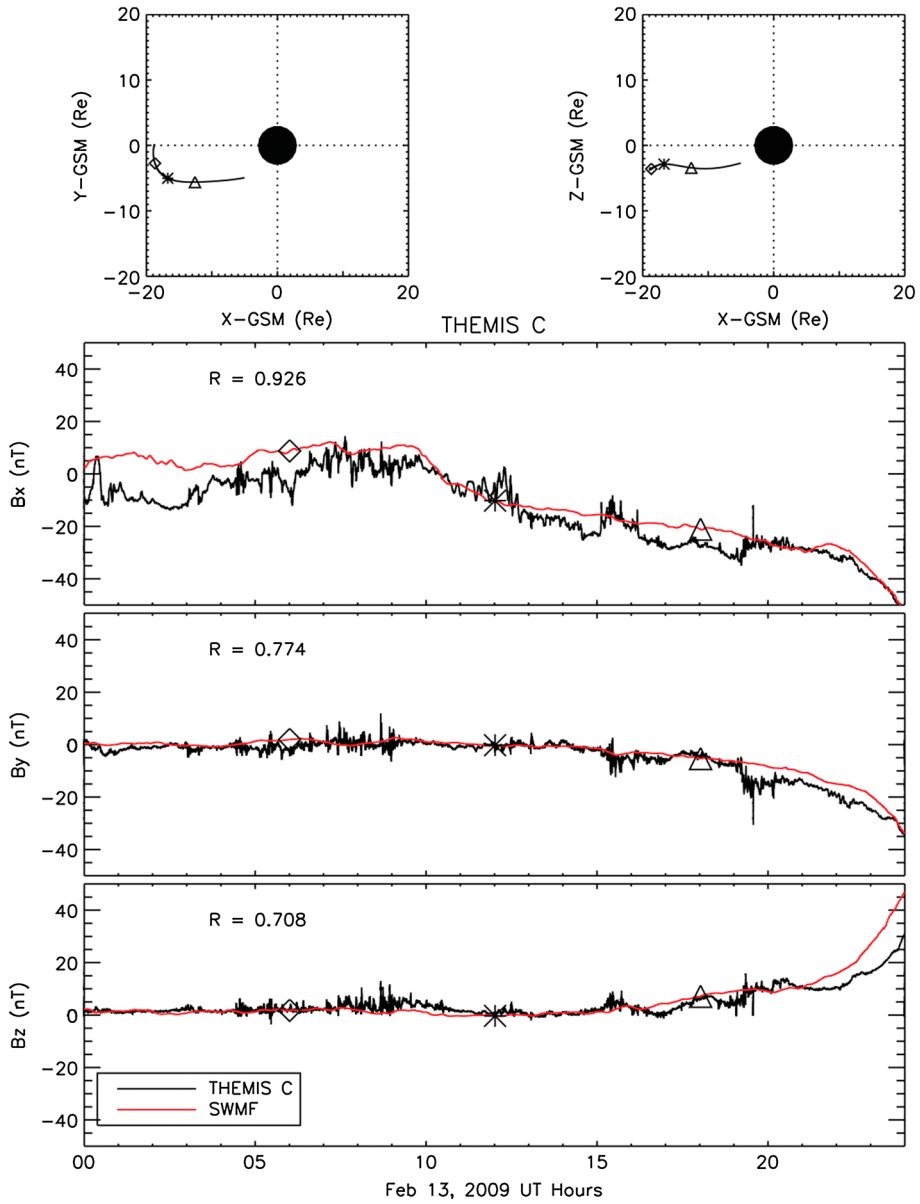

Figure 7. Comparison between the total magnetic field as output from SWMF magnetospheric modeling (red) and observed at THEMIS C (black) for 13 February 2009 interval. (top row) The spacecraft position in the $Y, Z = 0$ planes, followed by the magnetic field components as measured by the satellite (black lines) and predicted by the model (red lines). The green diamond, star, and triangle are used to show the satellite position and progression during the time interval presented here. Correlation coefficients between the observed and simulated values of B_x, B_y, and B_z are indicated in each of the corresponding panels.

region were situated within 1 h MLT and at distances between 7 and 10 R_E from the IB NOAA observations. However, there were ~40 IB observations between 2100 and 0300 MLT.

To accomplish this, we define an additional grid inside the MHD domain on which we trace all field lines and find the minimum value of magnetic field for each field line. At the location of minimum **B** we extract the MHD model parameters needed to calculate the *k* ratio. An illustration of this method is presented in Figure 8 which shows a side by side comparison between the magnetic field strength on the minimum **B** surface and SM $z = 0$ plane at 0403 UT on 13 February 2009 in our simulation. Calculation of the *k* ratio on the minimum **B** surface removes previous assumptions relating the magnetic equator with a planar surface (usually SM $z = 0$) as well as symmetry constraints on the geomagnetic field. For comparison purposes, we present here both views. A field line, traced from the observed location of NOAA 18 satellite at this time (Magnetic Latitude: −68.5°,

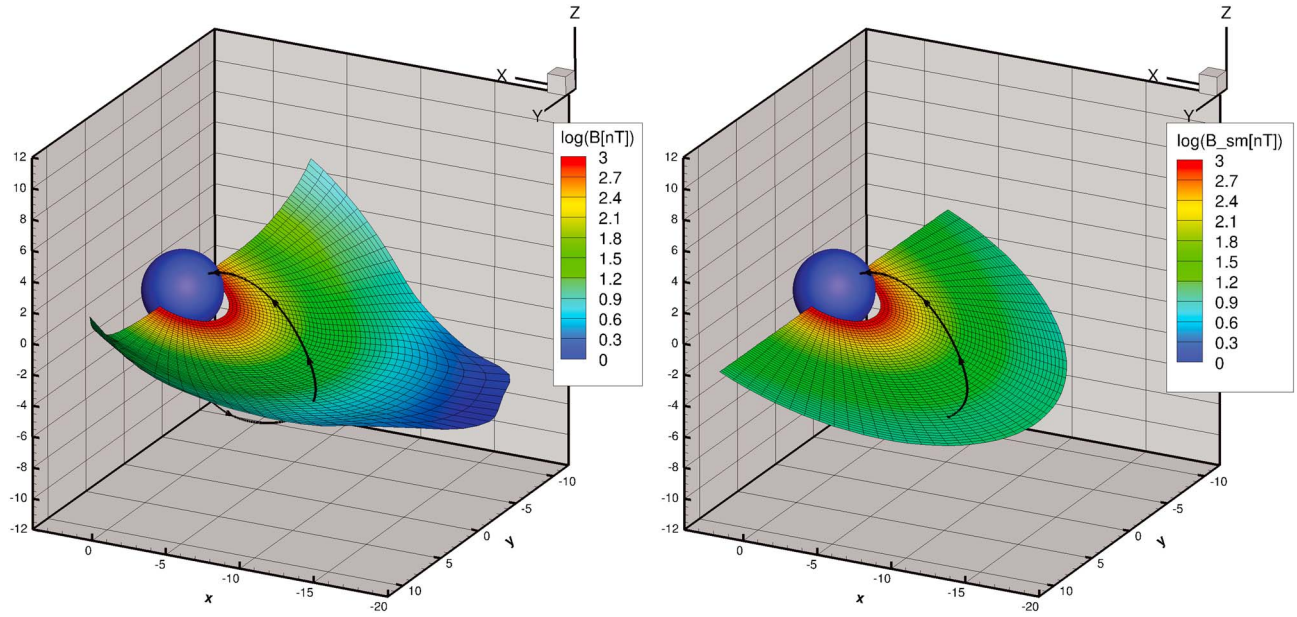

Figure 8. Magnetic field strength on the (left) minimum **B** surface and (right) SM $z = 0$ plane. The scale is logarithmic. A field line is traced from the location of NOAA 18 satellite 0403 UT in the simulation.

MLT: 22.88), crosses each of the two planes at different values of the magnetic field (at 7.8 nT on the minimum **B** surface versus 8.1 nT on the $z = 0$ SM plane).

At the next step, we calculate the $k = \frac{Rc}{\rho}$ ratio for a 30 keV energy particle in the magnetotail and whenever an isotropic boundary was observed by one of the NOAA satellites, we trace a field line from the location of the same satellite and locate its crossing in the magnetotail at the surfaces defined by the minimum **B** and by $z = 0$ in SM coordinates. The local properties of the total magnetic field at these crossings determine the conditions when the strong pitch angle scattering can occur.

7. Magnetic Field Lines for Selected IB Locations

Several isotropic boundaries were determined using the procedure developed and described by *Dubyagin et al.* [2013] based on NOAA observations during this time period. Two representative examples of $k = \frac{R_c}{\rho}$ ratio calculations based on SWMF simulation results are presented in Figures 9 and 10. Figure 9 shows a comparative view of the k ratio map for a 30 keV energy ion calculated on the minimum **B** surface (Figure 9, left) and SM $z = 0$ plane (Figure 9, right) at 0403 UT on 13 February 2009. At this time, isotropic boundaries were reported at the location of NOAA 18 corresponding to −68.5° in magnetic latitude (in the Northern Hemisphere) and 22.88 MLT. Therefore, a field line originating at the satellite location at this time is traced within the simulation domain. The value of the k ratio at the crossing of this field line with the surface of minimum **B** is 2.62, while the value of the k ratio at the field line crossing with SM $z = 0$ plane is 2.65. Since this is a quiet time interval and the IMF B_z at this time is only slightly negative but close to 0 nT, the magnetic field is dipole-like and the differences between the two planes on the nightside are only minimal.

In the same format as Figure 9, Figure 10 presents the simulation results corresponding to the 1257 UT time snapshot. At this time NOAA 17, located at −67.01° in magnetic latitude and 22.94 MLT, was recording similar fluxes of the precipitating and trapped ion populations, hence, an isotropic boundary. In the simulation results, we traced a field line starting at the location of NOAA 17 at this time and the value of k parameter at its crossing with the surface of minimum **B** is 80.88 while at the crossing with the SM $z = 0$ plane is 82.90. Again, the difference between values of k on the two surfaces is small.

To further check the model accuracy when resolving the magnetic field solution from SWMF, we identified several isotropic boundaries for which the magnetic field observations were available in conjunction with these NOAA auroral oval crossings. That is, we found several instances when the THEMIS A, D, and E spacecraft were located near the NOAA satellite in the MLT sector (±1 h) and at $r = 7–10\ R_e$, which are summarized in Table 1. This allows us to calculate a relative error parameter, $\Delta B = \frac{B^{\text{modeled}} - B^{\text{observed}}}{B^{\text{observed}}}$, where B^{modeled} represents

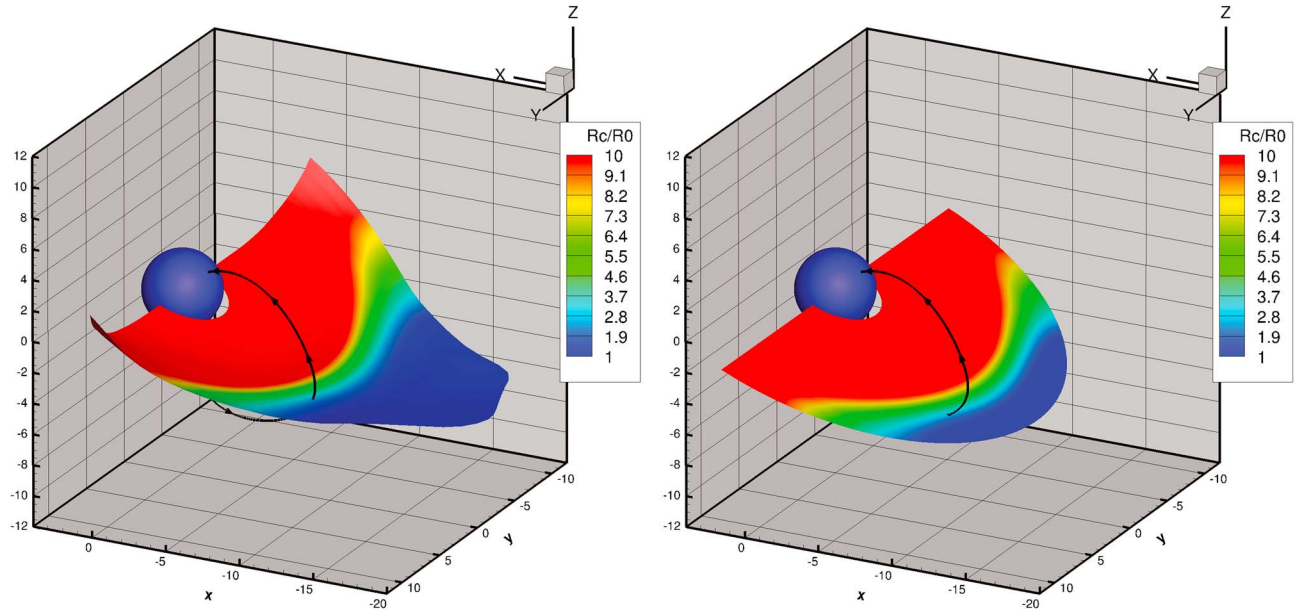

Figure 9. Comparative view of the values of $k = \frac{Rc}{\rho}$ ratio for a 30 keV energy ion calculated on the (left) minimum **B** surface and (right) SM $z = 0$ plane. The color scale is saturated at values of $k = 10$. A field line is traced from the location of NOAA 18 satellite 0403 UT in the simulation.

the magnetic field predicted by the model, while the B^{observed} represents its observed counterpart. The timing of the observed and modeled magnetic field, which corresponds to the time of the IB observation, is specified in Table 1. Figure 11 presents the dependence of the computed values of $k = \frac{R_c}{\rho}$ ratio on the accuracy parameter ΔB. Note that in this case, due to the fact that one isotropic boundary could be in conjugacy with more than one THEMIS observation, the k parameter is a multivalue function.

When $\Delta B < 0$, then $B_{\text{model}} < B_{\text{obs}}$ means that the model underestimates the tail currents and the model magnetic field line is less stretched than the observed field. Therefore, the $\frac{R_c}{\rho}$ ratio predicted by the model is larger than it should be leading to scattering to occur further down the tail. Conversely, when $\Delta B > 0$ then

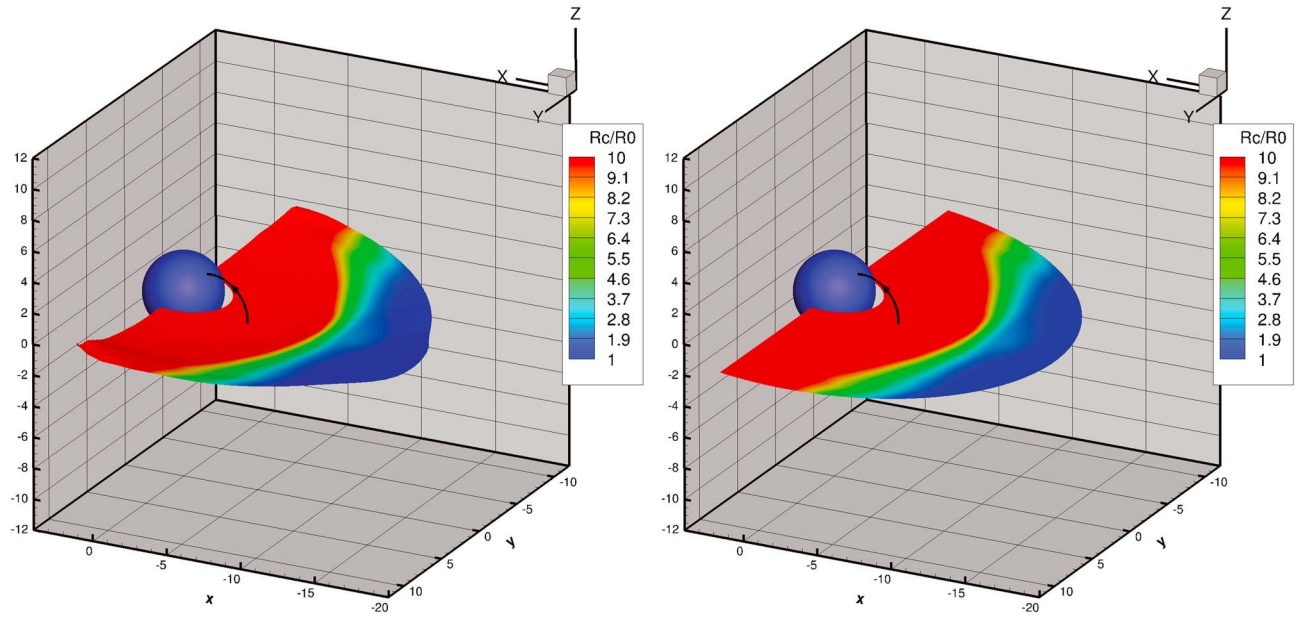

Figure 10. Comparative view of the values of $k = \frac{Rc}{\rho}$ ratio for a 30 keV energy ion calculated on the minimum **B** surface (left panel) and SM $z = 0$ plane (right panel). The color scale is saturated at values of $k = 10$. A field line is traced from the location of NOAA 17 satellite 1257 UT in the simulation.

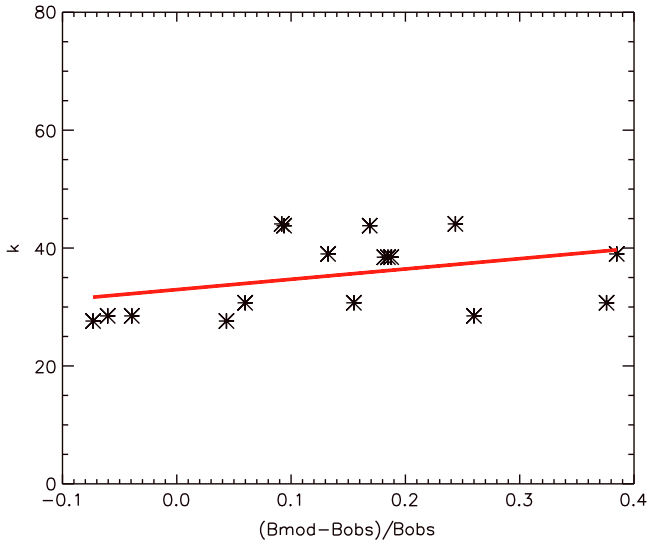

Figure 11. $k = \frac{Rc}{\rho}$ versus $\Delta B = \frac{B^{\text{modeled}} - B^{\text{observed}}}{B^{\text{observed}}}$ on the nightside ($0300 < MLT < 2100$) for 13 February 2009 quiet time period. The red line represents the linear fit $k = 32.95\Delta B + 17.5$.

$B_{\text{model}} > B_{\text{obs}}$; therefore, the model overestimates the field stretching, meaning that in the model, the scattering occurs closer to the Earth. The red line in the figure represents a linear fit of these data. Assuming perfect model prediction, that is, $\Delta B = 0$, then the scattering criterion is determined at the intersection of this fit. We find that the model setup used here predicts a $k = \frac{R_c}{\rho}$ ratio ~33. This value (and our analysis so far) states that in the absence of other scattering mechanisms, the strong pitch angle scattering takes place whenever the Larmor radius is ~33 smaller of magnitude of the radius of curvature. However, inspection of all IBs (not only the ones listed in Table 1) revealed that the value of k varies from low ($k \sim 2$ in Figure 9) to high ($k \sim 80$ in Figure 10).

8. Discussion

The *Sergeev et al.* [1983] study cites a critical value of the k parameter of $k_{CR} = 8$ for strong pitch angle scattering, with other works [e.g., *Sergeev and Tsyganenko*, 1982; *Delcourt et al.*, 1996] citing a range between 6 and 10 for k_{CR}. However, these studies assume definitions of k for which the minimum **B** is the value at the equator; therefore, the radius of curvature R_c and the gyroradius ρ are approximative and only dependent of the B_z component of the magnetic field. Also, the magnetic field outside the current sheet is tilted with respect to the equatorial plane by 45°, assuming $B_x = B_z$ outside the field reversal region. Therefore, the choice of $k_{CR} = 8$ could be model dependent and based on several assumptions involved in the numerical model. In this work, the radius of curvature and the gyroradius were calculated without any simplifications.

The IB latitude can be used as an indicator of total current strength only if there is no other competing scattering mechanism acting. Wave-particle interactions were long considered to be the main mechanism leading to pitch angle scattering of magnetospheric particles, and the measured particle precipitations were interpreted entirely in terms of this mechanism [e.g., *Hultqvist*, 1979]. Various wave-particle interaction processes can take place in the inner magnetosphere; therefore, scattering by fluctuating electromagnetic fields (EMIC waves) could also play a role in pitch angle diffusion since these waves can efficiently scatter the particles in the loss cone [e.g., *Erlandson and Ukhorskiy*, 2001; *Yahnin and Yahnina*, 2007]. However, there are some uncertainties in explaining the observed isotropic precipitation of energetic particles in terms of the wave-particle interaction mechanism [*Sergeev et al.*, 1993]. First, there is no sufficiently detailed picture of wave characteristics over the vast plasma sheet region where isotropic precipitation is observed. Second, even in cases when there is experimental information about waves, it is often not straightforward to decide whether they are able to produce the strong diffusion required to fill the loss cone isotropically.

In addition, wave intensity is, in general, structured and depends on the activity and certainty of particle fluxes, in sharp contrast to the observed properties of the isotropic precipitation of energetic particles [*Braysy et al.*, 1998; *Halford et al.*, 2010]. *Usanova et al.* [2012] reported on the low occurrence rate of EMIC waves on the

nightside inner magnetosphere during quiet times. Also, the preferential location for EMIC activity is dayside outer magnetosphere and it peaks during the storm main phase. Although unambiguous determination of the type of the isotropization mechanism from low-altitude observations is not possible, the likelihood that scattering by EMIC waves could lead to particle isotropization during the quiet time interval we selected is rather low. Inspection of ground-based observations reveals no wave activity between 2100 and 0300 MLT during this time (M. Usanova, personal communication, 2015). In addition, we inspected the energy-latitude dispersion of the IBs (those conjugated with THEMIS A, D, and E) to make sure that there were no anomalous dispersion events.

In order to evaluate adiabaticity, which is mainly controlled by the ratio between the radius of curvature and the particle's Larmor radius, we tested the threshold condition for strong pitch angle scattering. We found that in the absence of other scattering mechanisms, the strong pitch angle scattering takes place whenever the Larmor radius is within 2 orders of magnitude of the radius of curvature of the magnetic field. This means that the k parameter varies in a larger range ($2 < k < 85$) than previous studies suggested. Furthermore, our first-principles-based numerical model predicts a critical value of $k_{CR} \sim 33$. Our findings are supported by the high accuracy with which the numerical model, as represented by the high correlation coefficients and very low nRMSEs between the observed and modeled magnetic fields, resolves the geomagnetic field.

9. Conclusions

Produced in the near-equatorial region and controlled by the magnetic field in that region, low-altitude isotropy boundaries have the potential to carry information about field line mapping and therefore could provide a suitable tool to probe the mapping accuracy of magnetospheric models. Using a suite of SWMF models for the magnetospheric configuration, we determined what is the strong scattering threshold condition based on magnetic field solution from the MHD model and tested the conditions when the nightside particle precipitation is dominated by field line curvature scattering of central plasma sheet particles into the loss cone without including wave-particle interactions.

Magnetic field analysis based on data-model comparison reveals that the numerical simulation using the model setup presented here reproduced in great detail the observations from 12 different spacecraft, flying in the terrestrial magnetosphere during 13 February 2009. Therefore, based on the high correlation coefficients and very low nRMSEs between the components of the observed and simulated magnetic field at the satellite locations, we are confident that the model reproduces the magnetic field configuration with high accuracy. Having a realistic representation of the magnetic field is imperative since the scattering criterion, defined by the ratio between the radius of curvature and the particle gyroradius, is a function of the magnitude of the total magnetic field and its radius of curvature.

Our analysis predicts a $k = \frac{R_c}{\rho}$ ratio of ~33. However, we presented here two representative examples of when observed isotropic boundaries were found on magnetic field lines which crossed the equatorial plane at both low k and high k values. Our findings suggest that in the absence of other scattering mechanisms, the strong pitch angle scattering could take place whenever the particle gyroradius is within 2 orders of magnitude of the radius of curvature.

Acknowledgments
The authors would like to thank V. Sergeev for valuable discussions and suggestions. Work at the University of Michigan was performed with financial support from the National Aeronautics and Space Administration grants NASA award NNX14AF34G, NNX11A060G and NNX09AF45G and supported by the National Science Foundation under grant ATM-0802705. The work by N. Ganushkina and S. Dubyagin was also partly supported by the Academy of Finland and by the European Union Seventh Framework Programme (FP7/20072013) under grant agreements 606716 SPACESTORM and from the European Unions Horizon 2020 Research and Innovation Programme under grant agreement 637302 PROGRESS.
The authors would like to thank the Kyoto World Data Center for the *Dst* index and CDAWeb for allowing access to the plasma and magnetic field data. The NOAA/POES MEPED data are available at http://satdat.ngdc.noaa.gov/sem/poes/data/full. The data resulting from the numerical simulations are available upon request to the authors.

References

Alexeev, I. I., V. V. Kalegaev, E. S. Belenkaya, S. Y. Bobrovnikov, Y. I. Feldstein, and L. I. Gromova (2001), Dynamic model of the magnetosphere: Case study for January 9–12, 1997, *J. Geophys. Res.*, *106*, 25,683–25,694, doi:10.1029/2001JA900057.

Asikainen, T., V. Maliniemi, and K. Mursula (2010), Modeling the contributions of ring, tail, and magnetopause currents to the corrected *Dst* index, *J. Geophys. Res.*, *115*(A), A12203, doi:10.1029/2010JA015774.

Blockx, C., J. C. Gérard, M. Meurant, B. Hubert, and V. Coumans (2005), Far ultraviolet remote sensing of the isotropy boundary and magnetotail stretching, *J. Geophys. Res.*, *110*, A11215, doi:10.1029/2005JA011103.

Blockx, C., J. C. Gérard, V. Coumans, B. Hubert, and M. Meurant (2007), A comparison between FUV remote sensing of magnetotail stretching and the T01 model during quiet conditions and growth phases, *Ann. Geophys.*, *25*(1), 161–170.

Braysy, T., K. Mursula, and G. Marklund (1998), Ion cyclotron waves during a great magnetic storm observed by Freja double-probe electric field instrument, *J. Geophys. Res.*, *103*(A3), 4145–4155.

Buechner, J., and L. M. Zelenyi (1987), Chaotization of the electron motion as the cause of an internal magnetotail instability and substorm onset, *J. Geophys. Res.*, *92*(A12), 13,456–13,466.

De Zeeuw, D. L., S. Sazykin, R. A. Wolf, T. I. Gombosi, A. J. Ridley, and G. Toth (2004), Coupling of a global MHD code and an inner magnetospheric model: Initial results, *J. Geophys. Res.*, *109*, A12219, doi:10.1029/2003JA010366.

Delcourt, D. C., J. A. Sauvaud, R. F. Martin, and T. E. Moore (1996), On the nonadiabatic precipitation of ions from the near-Earth plasma sheet, *J. Geophys. Res.*, *101*(A8), 17,409–17,418.

Donovan, E., B. Jackel, D. Klumpar, and R. Strangeway (2003a), Energy dependence of the isotropy boundary latitude, in *Proc. of Atmos. Studies by Optical Methods*, vol. 92, pp. 11–14.

Donovan, E. F., B. J. Jackel, I. Voronkov, T. Sotirelis, F. Creutzberg, and N. A. Nicholson (2003b), Ground-based optical determination of the b2i boundary: A basis for an optical MT-index, *J. Geophys. Res.*, *108*(A3), 1115, doi:10.1029/2001JA009198.

Dubyagin, S., N. Ganushkina, S. Apatenkov, M. Kubyshkina, H. Singer, and M. Liemohn (2013), Geometry of duskside equatorial current during magnetic storm main phase as deduced from magnetospheric and low-altitude observations, *Ann. Geophys.*, *31*(3), 395–408.

Erlandson, R. E., and A. J. Ukhorskiy (2001), Observations of electromagnetic ion cyclotron waves during geomagnetic storms: Wave occurrence and pitch angle scattering, *J. Geophys. Res.*, *106*(A3), 3883–3895.

Fritz, T. A. (1970), Study of the high-latitude, outer-zone boundary region for ≥40-kev electrons with satellite Injun 3, *J. Geophys. Res.*, *75*(28), 5387–5400.

Ganushkina, N., T. Pulkkinen, M. Kubyshkina, H. Singer, and C. Russell (2004), Long-term evolution of magnetospheric current systems during storms, *Ann. Geophys.*, *22*, 1317–1334, doi:10.5194/angeo-22-1317-2004.

Ganushkina, N. Y., T. I. Pulkkinen, M. V. Kubyshkina, V. A. Sergeev, E. A. Lvova, T. A. Yahnina, A. G. Yahnin, and T. Fritz (2005), Proton isotropy boundaries as measured on mid- and low-altitude satellites, *Ann. Geophys.*, *23*(5), 1839–1847.

Ganushkina, N. Y., M. W. Liemohn, M. V. Kubyshkina, R. Ilie, and H. J. Singer (2010), Distortions of the magnetic field by storm-time current systems in Earth's magnetosphere, *Ann. Geophys.*, *28*, 123–140, doi:10.5194/angeo-28-123-2010.

Gilson, M. L., J. Raeder, E. Donovan, Y. S. Ge, and S. B. Mende (2011), Statistics of the longitudinal splitting of proton aurora during substorms, *J. Geophys. Res.*, *116*, A08226, doi:10.1029/2011JA016640.

Gilson, M. L., J. Raeder, E. Donovan, Y. S. Ge, and L. Kepko (2012), Global simulation of proton precipitation due to field line curvature during substorms, *J. Geophys. Res.*, *117*, A05216, doi:10.1029/2012JA017562.

Glocer, A., G. Tóth, Y. Ma, T. Gombosi, J.-C. Zhang, and L. M. Kistler (2009), Multifluid block-adaptive-tree solar wind roe-type upwind scheme: Magnetospheric composition and dynamics during geomagnetic storms: Initial results, *J. Geophys. Res.*, *114*, A12203, doi:10.1029/2009JA014418.

Gombosi, T. I., G. Tóth, D. L. De Zeeuw, K. C. Hansen, K. Kabin, and K. G. Powell (2002), Semirelativistic magnetohydrodynamics and physics-based convergence acceleration, *J. Comput. Phys.*, *177*, 176–205, doi:10.1006/jcph.2002.7009.

Halford, A. J., B. J. Fraser, and S. K. Morley (2010), EMIC wave activity during geomagnetic storm and nonstorm periods: CRRES results, *J. Geophys. Res.*, *115*, A12248, doi:10.1029/2010JA015716.

Harel, M., R. A. Wolf, P. H. Reiff, R. W. Spiro, W. J. Burke, F. J. Rich, and M. Smiddy (1981), Quantitative simulation of a magnetospheric substorm: I. Model logic and overview, *J. Geophys. Res.*, *86*, 2217–2241, doi:10.1029/JA086iA04p02217.

Hultqvist, B. (1979), The hot ion component of the magnetospheric plasma and some relations to the electron component—Observations and physical implications, *Space Sci. Rev.*, *23*(4), 581–675.

Ilie, R., M. W. Liemohn, J. Borovsky, and J. Kozyra (2010a), An investigation of the magnetosphere-ionosphere response to real and idealized CIR events through global MHD simulations, *Proc. R. Soc. A*, *466*(2123), 3279–3303, doi:10.1098/rspa.2010.0074.

Ilie, R., M. W. Liemohn, and A. Ridley (2010b), The effect of smoothed solar wind inputs on global modeling results, *J. Geophys. Res.*, *115*, A01213, doi:10.1029/2009JA014443.

Ilie, R., R. M. Skoug, P. Valek, H. O. Funsten, and A. Glocer (2013), Global view of inner magnetosphere composition during storm time, *J. Geophys. Res. Space Physics*, *118*, 7074–7084.

Ilie, R., M. W. Liemohn, G. Toth, N. Yu Ganushkina, and L. K. S. Daldorff (2015), Assessing the role of oxygen on ring current formation and evolution through numerical experiments, *J. Geophys. Res. Space Physics*, *120*, 4656–4668, doi:10.1002/2015JA021157.

Kubyshkina, M., V. Sergeev, N. Tsyganenko, V. Angelopoulos, A. Runov, H. Singer, K. H. Glassmeier, H. U. Auster, and W. Baumjohann (2009), Toward adapted time-dependent magnetospheric models: A simple approach based on tuning the standard model, *J. Geophys. Res.*, *114*, A00C21, doi:10.1029/2008JA013547.

Liemohn, M. W., D. L. De Zeeuw, R. Ilie, and N. Y. Ganushkina (2011), Deciphering magnetospheric cross-field currents, *Geophys. Res. Lett.*, *38*, L20106, doi:10.1029/2011GL049611.

Lvova, E. A., V. A. Sergeev, and G. R. Bagautdinova (2005), Statistical study of the proton isotropy boundary, *Ann. Geophys.*, *23*(4), 1311–1316.

Meng, X., G. Tóth, M. W. Liemohn, T. I. Gombosi, and A. Runov (2012), Pressure anisotropy in global magnetospheric simulations: A magnetohydrodynamics model, *J. Geophys. Res.*, *117*, A08216, doi:10.1029/2012JA017791.

Meurant, M., J. C. Gérard, C. Blockx, E. Spanswick, E. F. Donovan, B. Hubert, V. Coumans, and M. Connors (2007), EL—A possible indicator to monitor the magnetic field stretching at global scale during substorm expansive phase: Statistical study, *J. Geophys. Res.*, *112*, A05222, doi:10.1029/2006JA012126.

Powell, K. G., P. L. Roe, T. J. Linde, T. I. Gombosi, and D. L. De Zeeuw (1999), A solution-adaptive upwind scheme for ideal magnetohydrodynamics, *J. Comput. Phys.*, *154*, 284–309, doi:10.1006/jcph.1999.6299.

Ridley, A., T. Gombosi, and D. Dezeeuw (2004), Ionospheric control of the magnetosphere: Conductance, *Ann. Geophys.*, *22*, 567–584.

Ridley, A. J., and M. W. Liemohn (2002), A model-derived storm time asymmetric ring current driven electric field description, *J. Geophys. Res.*, *107*(A8), 1151, doi:10.1029/2001JA000051.

Sandel, B. R., et al. (2000), The extreme ultraviolet imager investigation for the IMAGE mission, *Space Sci. Rev.*, *91*(1), 197–242.

Sergeev, V. A., and B. B. Gvozdevsky (1995), MT-index: A possible new index to characterize the magnetic configuration of magnetotail, *Ann. Geophys.*, *13*(10), 1093–1103, doi:10.1007/s00585-995-1093-9.

Sergeev, V. A., and N. A. Tsyganenko (1982), Energetic particle losses and trapping boundaries as deduced from calculations with a realistic magnetic-field model, *Planet. Space Sci.*, *30*(10), 999–1006.

Sergeev, V. A., E. M. SAZHINA, N. A. Tsyganenko, J. A. LUNDBLAD, and F. SORAAS (1983), Pitch-angle scattering of energetic protons in the magnetotail current sheet as the dominant source of their isotropic precipitation into the nightside ionosphere, *Planet. Space Sci.*, *31*(10), 1147–1155.

Sergeev, V. A., M. Malkov, and K. Mursula (1993), Testing the isotropic boundary algorithm method to evaluate the magnetic field configuration in the tail, *J. Geophys. Res.*, *98*(A5), 7609–7620.

Sergeev, V. A., T. I. Pulkkinen, T. I. Pellinen, and N. A. Tsyganenko (1994), Hybrid state of the tail magnetic configuration during steady convection events, *J. Geophys. Res.*, *99*(A12), 23,571–23,582.

Sergeev, V. A., S. A. Chernyaeva, S. V. Apatenkov, N. Y. Ganushkina, and S. V. Dubyagin (2015), Energy-latitude dispersion patterns near the isotropy boundaries of energetic protons, *Ann. Geophys.*, *33*, 1059–1070.

Toffoletto, F., S. Sazykin, R. Spiro, and R. Wolf (2003), Inner magnetospheric modeling with the rice convection model, *Space Sci. Rev.*, *107*, 175–196, doi:10.1023/A:1025532008047.

Tóth, G., Y. Ma, and T. I. Gombosi (2008), Hall magnetohydrodynamics on block-adaptive grids, *J. Comput. Phys.*, *227*, 6967–6984, doi:10.1016/j.jcp.2008.04.010.

Tóth, G., et al. (2005), Space weather modeling framework: A new tool for the space science community, *J. Geophys. Res.*, *110*, A12226, doi:10.1029/2005JA011126.
Tóth, G., et al. (2012), Adaptive numerical algorithms in space weather modeling, *J. Comput. Phys.*, *231*, 870–903, doi:10.1016/j.jcp.2011.02.006.
Tsyganenko, N. A. (1982), Pitch-angle scattering of energetic particles in the current sheet of the magnetospheric tail and stationary distribution-functions, *Planet. Space Sci.*, *30*(5), 433–437.
Tsyganenko, N. A. (1995), Modeling the Earth's magnetospheric magnetic field confined within a realistic magnetopause, *J. Geophys. Res.*, *100*, 5599–5612, doi:10.1029/94JA03193.
Tsyganenko, N. A. (2002), A model of the near magnetosphere with a dawn-dusk asymmetry: 1. Mathematical structure, *J. Geophys. Res.*, *107*(A8), 1179, doi:10.1029/2001JA000219.
Tsyganenko, N. A., and M. I. Sitnov (2005), Modeling the dynamics of the inner magnetosphere during strong geomagnetic storms, *J. Geophys. Res.*, *110*, A03208, doi:10.1029/2004JA010798.
Usanova, M. E., I. R. Mann, J. Bortnik, L. Shao, and V. Angelopoulos (2012), THEMIS observations of electromagnetic ion cyclotron wave occurrence: Dependence on *AE*, *SYM-H*, and solar wind dynamic pressure, *J. Geophys. Res.*, *117*, A10218, doi:10.1029/2012JA018049.
Welling, D. T., and M. W. Liemohn (2014), Outflow in global magnetohydrodynamics as a function of a passive inner boundary source, *J. Geophys. Res. Space Physics*, *119*, 2691–2705.
Yahnin, A. G., and T. A. Yahnina (2007), Energetic proton precipitation related to ion-cyclotron waves, *J. Atmos. Sol. Terr. Phys.*, *69*(14), 1690–1706.
Yu, Y., and A. J. Ridley (2009), Response of the magnetosphere-ionosphere system to a sudden southward turning of interplanetary magnetic field, *J. Geophys. Res.*, *114*, A03216, doi:10.1029/2008JA013292.
Zhang, J., et al. (2007), Solar and interplanetary sources of major geomagnetic storms during 1996–2005, *J. Geophys. Res.*, *112*, A10102, doi:10.1029/2007JA012321.